J Mater Sci (2020) 55:9608–9622

Metals & corrosion

Microstructural effects on central crack formation in hot cross-wedge-rolled high-strength steel parts

Xianyan Zhou[1], Zhutao Shao[1], Famin Tian[2], Christopher Hopper[1], and Jun Jiang[1,*]

[1] Department of Mechanical Engineering, Imperial College London, Exhibition Road, London SW7 2AZ, UK
[2] Dyson School of Design Engineering, Imperial College London, Imperial College Road, London SW7 1AL, UK

Received: 10 March 2020
Accepted: 11 April 2020
Published online: 22 April 2020

ABSTRACT

Central cracking in cross-wedge-rolled workpieces results in high wastage and economic loss. Recent cross-wedge rolling tests on two batches of steel showed that one batch formed central cracks, while the other was crack-free. The batches were both nominally of the same chemical composition and thermomechanical treatment history. In addition, both batches had passed all the standard quality assessments set for conventional forging processes. It was suspected that the different cracking behaviours were due to differences in microstructure between the two as-received steel billets, and the material in cross-wedge rolling (CWR) was more sensitive to the initial microstructure compared with other forging processes due to its specific loading condition including ostensibly compression and large plastic strain. Nevertheless, no previous study of this important problem could be identified. The aim of this study is, therefore, to identify the key microstructural features determining the central crack formation behaviour in CWR. The hot workability of the as-received billets was studied under uni-axial tensile conditions using a Gleeble 3800 test machine. Scanning electron microscope with energy-dispersive X-ray spectroscopy and electron backscatter diffraction was applied to characterise, quantitatively analyse, and compare the chemical composition, phase, grain, and inclusions in these two billets, both at room temperature and also at the CWR temperature (1080 °C). Non-metallic inclusions (oxides, sulphides, and silicates) in the billets were determined to be the main cause of the reported central cracking problem. The ductility of the steels at both room and elevated temperatures deteriorated markedly in the presence of the large volumes of inclusions. Grain boundary embrittlement occurred at the CWR temperature due to the aggregation of inclusions along the grain boundaries. It is suggested that a standard on specifying the inclusion quantity and size in CWR billets be established to produce crack-free products.

Address correspondence to E-mail: jun.jiang@imperial.ac.uk

https://doi.org/10.1007/s10853-020-04677-5

Introduction

Cross-wedge rolling (CWR) is widely used to manufacture axially symmetric products, such as the camshafts, gear shafts, or preforms for forging [1]. The formation of central cracks (i.e. the cavities formed in the centre of the workpiece), also known as the Mannesmann effect, was acknowledged as the most common defect limiting the development of CWR [2]. To drive further development of CWR into areas such as the more safety-critical aerospace industry, it is of great importance to understand the fracture mechanisms of central crack formation and determine a proper fracture criterion or damage model to produce crack-free CWR products. The research in this area is globally active and ongoing. Pater et al. [3] compared nine fracture criteria to find the one most suitable for the prediction of central crack formation. Yang et al. [4] studied central crack formation on a microstructural scale and revealed the ductile fracture mechanism of steels at high temperature. Zhou et al. [5] considered the combined effects of the shear and normal stress and proposed a novel fracture criterion, which was validated quantitively. However, there is not an agreement on the fracture mechanisms of central crack formation due to the complex mechanical and microstructural behaviours during CWR.

It is well known that the workability of a material is usually determined by two factors: the process-related parameters (including die geometries, thermal history, strain rate, etc.) and the material-related parameters (such as phase composition, grain size, and chemical composition). Intensive studies have been conducted to investigate the effects of stress states on central crack formation. Dong et al. [6] used finite element methods to analyse the stress distribution during CWR and determine the cause of central cracks. Li et al. [7] systematically investigated central crack formation under various die geometries and proposed a non-dimensional fracture criterion for producing central crack-free products. By adopting the Cockcroft–Latham damage model, Pater concluded that using a large forming angle and small spreading angle during CWR could effectively avoid central cracking [8]. After careful analysis of the shear and tensile deformation at the central region of the workpiece during CWR, Yang et al. [4] suggested that the forming angle had the greatest effect on central crack formation. Although many studies have been conducted to analyse the effects of process parameters (e.g. die geometries), however, limited attention has been devoted to understanding the effects of material-related parameters (grain size, phase, and chemical composition) on the central crack formation problem. Thus, in order to control central crack formation accurately and efficiently, it is necessary to understand the microstructure evolution during CWR and determine the critical microstructural feature for central crack formation.

Cross-wedge rolling companies previously found that when using the same working process-related parameters (i.e. die geometry, thermal history, and strain rate), central cracks were frequently observed in some batches of the CWR-formed steel parts, but not in other batches, even though the batches had the same nominal chemical composition [9]. The initial steel feedstock billets met all the typical technical specifications required, including strength, ductility, chemical composition, and porosity. It is, therefore, of great interest to investigate which material-related parameters may influence central crack formation, and the mechanisms involved. Cross-wedge rolling companies suffer heavy losses due to this problematic phenomenon. In discovering the material-related fracture mechanisms and proposing possible solutions to mitigate the risk of cracking, it is thought that the findings from this study could have a large beneficial impact on the CWR industry.

Some studies have been conducted to understand the microstructure distribution and evolution during CWR. For example, Wang et al. [10] studied AISI 5140 steel both numerically and experimentally, considering phase transformation, grain recrystallisation, and grain growth. Huo et al. [11] established a unified constitutive model coupling microstructure and ductile damage to predict the microstructure evolution and damage distribution. Nevertheless, limited understanding of the key microstructural features of central crack formation has been gained.

The workability of steel under warm and hot forming conditions is greatly affected by microstructural features such as inclusions, grain size, phase, and carbides. In some cases, inclusions were found to be detrimental to the mechanical properties [12–14]. The size and distribution of inclusions are of great importance to the workability of steel [15–17]. The fracture mechanisms caused by inclusions in stainless steels was revealed [15]. Under deformation, microvoids, cracks, and decohesion

formed around these inclusions due to the mismatch of elastic and thermal properties within the matrix. The microcracks formed could subsequently link up and lead to fracture in the material. It has been reported that the common inclusions in steels such as alumina (Al_2O_3), manganese sulphide (MnS), and spinel (mainly MgO–Al_2O_3) are mostly formed during the steel melting-casting stage, or are introduced in the calcium treatment, as in the case of calcium aluminates ($xCaO$–yAl_2O_3) [18, 19]. It was studied that Al_2O_3 inclusions are prone to form clusters during hot rolling [20, 21]. These clusters break into stringers and lead to anisotropy of toughness and ductility, as further substantiated by Ma et al. [22]. MnS inclusions are softer than the surrounding steel matrix, and during hot rolling, they tend to elongate along the rolling direction and cause in-plane anisotropy [12, 20, 23, 24].

Aside from these inclusions, the grain size effects are also significant. Crowther and Mintz [25] and Mintz et al. [26] discovered that a smaller grain size could typically increase the hot formability of some steels. Kim et al. [27] found that this effect became negligible when the final fracture could be attributed to precipitates. Phases, in terms of morphology and volume fraction, affect the hot workability of steels [28]. Marder and Bramfitt [29] found that the interlamellar spacing of pearlites was inversely related to both the yield strength and the fracture strength. Elwazri et al. [30] observed that the ductility of hypereutectoid steel was related to the pearlite colony size. Further, Kammerhofer et al. [31] found that the fully spheroidised microstructure in pearlitic steel could reduce the strength but, remarkably, also increase the fracture toughness. Kulakov et al. [32] found that different phase components (ferrite, pearlite, bainite, or martensite) in dual-phase steels affected the recrystallisation and austenite formation process. The interaction between recrystallisation and austenitic transformation during intercritical annealing of cold-rolled DP steels was revealed by Zheng and Raabe [33]. This interaction affected the morphology and spatial distribution of the austenite. However, as CWR is a complex problem involving many variables at a microscopic scale, no comprehensive study has been found which identifies the microstructural factors critical to the formation of central cracks in steels during CWR.

The aim of this study, therefore, is to investigate the microstructural factors associated with central crack formation. The material studied is a gear shaft steel, namely 20NiCr3H steel. Two characteristic batches of steel samples were selected. The selection was based on whether or not central cracks were found in cross-wedge-rolled parts formed using the batch. The mechanical behaviour of the two sample batches was evaluated at both room and elevated temperature using a Gleeble 3800 testing machine. Four microscopic variables, potentially relevant in central crack formation (inclusions, chemical compositions, phase, and grain size), were then studied and compared in detail. From these studies, the key variables and fracture mechanisms were determined, and possible solutions for mitigating this problem were proposed.

Materials and methodology

Material description

Two 20NiCr3H steel samples were supplied by Helai Ltd. A representative axial section along with the typical microstructure at the central region is illustrated in Fig. 1. The samples were taken from two different steel billets, Billet 1 and Billet 2. Billet 1 was selected from the batch of steel that was not found to exhibit central cracking, while Billet 2 was selected from a different batch that had produced cracked products, as shown in Fig. 1b1, b2. Both samples exhibited similar phase compositions, pearlite and ferrite. The nominal chemical compositions of the steels are presented in Table 1. These two batches of steel billets were manufactured by the same process (continuous casting and rolling). The total weight of each batch was around 50 tonnes. To confirm the consistency of central crack formation in each batch, 100 billets from each batch were selected and processed using the same CWR process, that is, the billets were first heated to 1080 °C in a furnace within 65 s for austenisation, then placed in a CWR machine (H1200) with the same tools (forming angle 30°, stretching angle 7.5°, and area reduction ratio of 58%) at the same rolling speed (20 m/min). After rolling, all of the CWR products were cooled in the air, followed by ultrasonic flaw testing to inspect for central cracks. The 100 billets from Batch 1 did not show any central cracks, while those from Batch 2 were all centrally cracked.

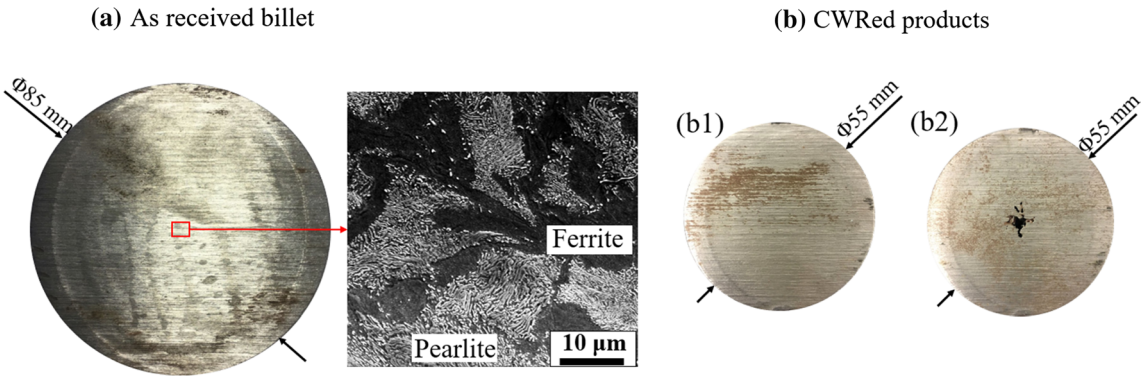

Figure 1 As-received materials: **a** the axial cross section of one billet along with the SEM characterised microstructure at the central region; **b1**, **b2** the CWR-formed axial products from Billets 1 and 2, respectively.

Table 1 The nominal chemical compositions of the steel 20CrNi3H [34]

Chemical compositions	C	Si	Mn	P	S	Cr	Ni	Cu	[O]
GB/T5216-85	0.17/0.23	0.17/0.37	0.30/0.65	≤ 0.035	≤ 0.035	0.60/0.95	2.70/3.25	≤ 0.20	≤ 20 ppm

Thermal mechanical tests

The mechanical properties of two billets at both room temperature and at the hot rolling temperature of 1080 °C were determined from uniaxial tensile tests using a Gleeble 3800 test machine. The tensile test specimen geometry and location in the billet cross section is illustrated in Fig. 2a. For the tests under hot rolling conditions the specimens were heated to 1080 °C within 65 s (at a heating rate of 16.2 °C/s), then pulled to fracture at a strain rate of 1/s. The samples were cooled down in the air. A thermocouple was spot welded on the surface of the central region of the specimen to record and control the temperature. A dilatometer was applied to record the width change during the tests. The above process was repeated for the tensile test at room temperature with the same sample geometry and strain rate, but without any heating process. At least three tests at room temperature and at 1080 °C were conducted to ensure the repeatability of the obtained results.

Heat treatment process

The same thermal profile was applied to replicate the preheating stage of CWR to investigate the preheated microstructure changes prior to plastic deformation. Samples of dimensions 5 × 5 × 3 mm were cut from the central regions of both Billets 1 and 2, indicated as the A0 region in Fig. 2b. The samples were heated to

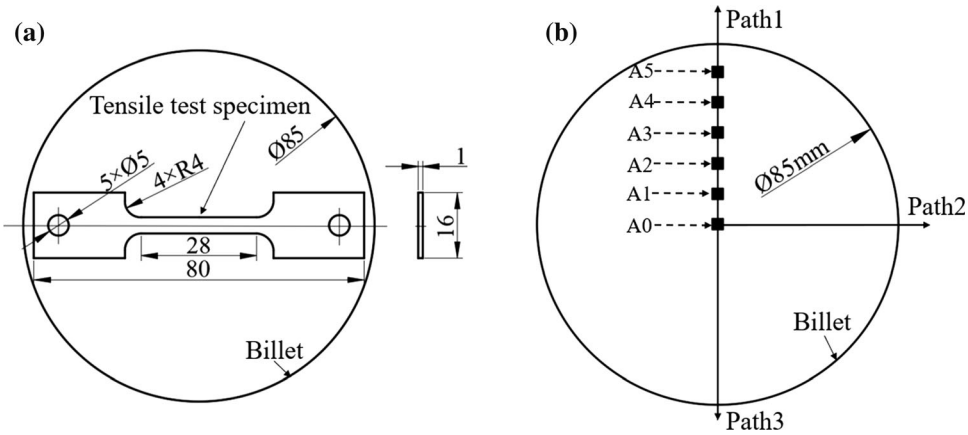

Figure 2 Schematic illustration of **a** geometry and location of the tensile testing specimen on the billets and **b** the regions of interest on the transverse section of the billet.

1080 °C and held for 65 s in a preheated furnace, then were immediately water quenched to freeze the formed microstructure.

Material characterisation

Samples taken from the test specimens were ground with grinding papers from P800 to P4000, followed by 1 μm diamond suspension polishing. The polished sample surfaces were then etched by the 2% nital for approximately 20 s to reveal the phase structure. For electron backscatter diffraction (EBSD) characterisation, the samples were polished further via colloidal silica suspension for 20 min.

The inclusions in the samples were characterised using optical microscope and scanning electron microscope (SEM) images. To quantify the statistic distribution of the inclusions, Image J software [35] was used to detect inclusions based on the high contrast between the steel matrix and inclusions. Scanning electron microscopy with energy-dispersive X-ray spectroscopy (SEM/EDX) was applied to identify the chemical composition of inclusions.

SEM/EDX was also used to identify the chemical elements, Ni, Cr, and Mn, and quantitatively analyse their distribution across the transverse section (from A0 to A5 along three paths, Fig. 2b). Three points/maps were taken at each area, and the average values were calculated to observe their distribution across the transverse section.

The phase and grain size evolution were characterised using the Bruker Esprit EBSD system. The SEM operating voltage was 25 kV, the magnification was set at 500×, and the scanning step size was set at 0.5 μm. The postprocess for phase identification was carried out using Atex software [36]. A 15° misorientation between adjacent points was set as the grain boundary definition. No smoothing process was applied to these obtained EBSD maps.

Results

Thermal mechanical tests

Stress–strain curves

The stress–strain curves for the two billets at room temperature and at 1080 °C are compared in Fig. 3. The specimen fracture areas are displayed as insets.

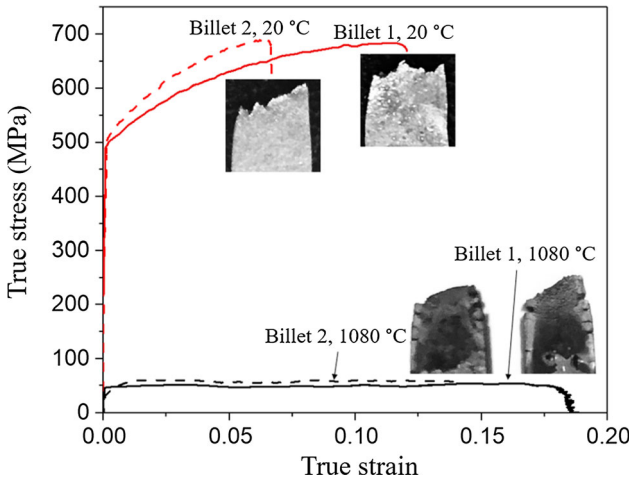

Figure 3 True stress—true strain curves of the two billets at room temperature and rolling temperature.

The ductility of Billet 1 (crack-free) was considerably higher than that of Billet 2 (central cracked), both at room temperature and at elevated temperature. At room temperature, the fracture strain of Billet 2 was approximately 50% lower than that of Billet 1—0.07 and 0.12, respectively. At elevated temperature, the ductility of both samples increased significantly. The fracture strain of Billet 2 doubled, but it was still only about 75% of that of Billet 1. Although the difference in ductility between two samples was significant, it is interesting to note that their flow stress levels were similar. At room temperature, the yield strengths were almost the same, at approximately 490 MPa, and the ultimate strengths were 685 and 690 MPa, for Billets 1 and 2, respectively. At 1080 °C, the yield strength of Billet 2 was 46 MPa, with an ultimate strength of 60 MPa, slightly higher than that of Billet 1 (54 MPa).

Fracture surface

Figure 4 presents the fracture micrographs from the tensile specimens. Ductile fracture was observed in billets deformed and fractured at room temperature, and intergranular fracture was found at elevated temperature. According to Fig. 4a, b, large numbers of dimples and cracks were observed in both specimens, indicating ductile fracture at room temperature in both billets. The clear regular patterns show that the cracks were prone to propagate through the thickness direction, as indicated by the blue arrows in Fig. 4a, b. This corresponds to the axial direction of the as-received billets. A closer look reveals that large

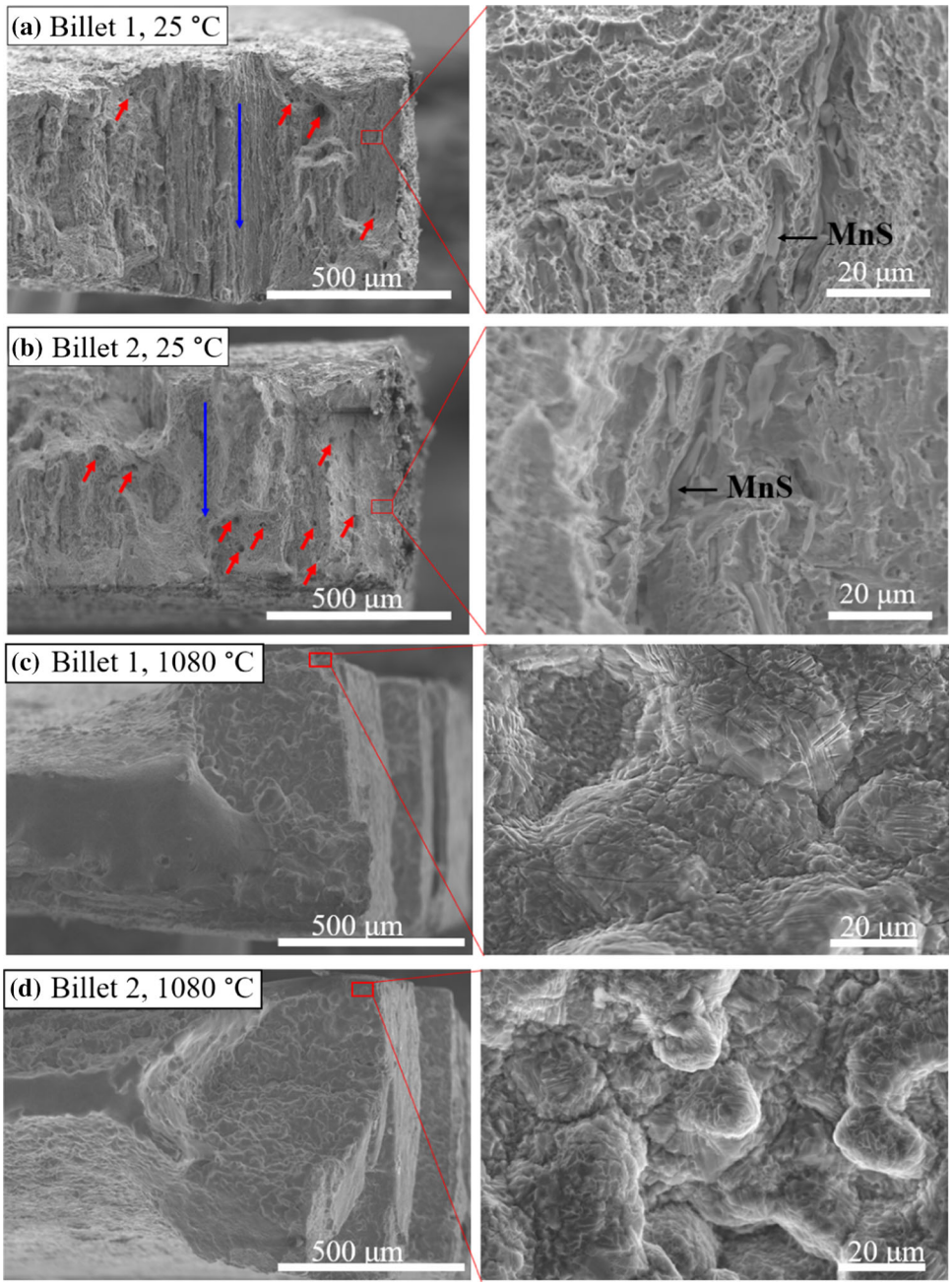

Figure 4 Fractography of two billets at room temperature and at 1080 °C.

and elongated inclusions were scattered throughout. These were identified as MnS by using SEM/EDX. When comparing the room temperature fracture surfaces of the two billets, it is clear that the fracture surface of Billet 2 was rougher, and the crack propagating paths were more random, whereas the cracks in Billet 1 propagated mainly along the thickness direction. This may point to the greater presence of MnS inclusions formed in Billet 2.

At elevated temperature, intergranular fracture occurred in both billets, as shown in Fig. 4c, d. The fracture nucleated on the transverse section, then propagated along the loading direction, and finally failed along the transverse section. Unlike the rough surface at room temperature, here, the fracture surfaces were relatively smooth. Large particles were observed, and higher magnification images indicate these may be austenite grains. The austenite grains observed in Billet 2 were significantly smaller than those in Billet 1. This may be due to constrained dynamic recrystallisation in Billet 2 resulting from the inclusions hindering grain growth.

The longitudinal section of the fracture tips for the two elevated temperature samples is shown in Fig. 5. A comparison of the macroscopic images in Fig. 5a, b reveals intensive secondary cracks in Billet 1. In both cases, the cracks propagated along the same direction, normal to the loading direction. Under a higher magnification, as depicted in Fig. 5c, it is clear that the crack edges were not strictly normal to the loading direction, but were distributed along the prior austenite grain boundaries, confirming the intergranular nature of the fracture. A layer of iron oxides between the crack and the steel matrix is also observed. This layer is suspected to have been formed after the tensile test, possibly during the sample preparation process, as steel tends to oxide easily in the air. Through observing the gap between the iron oxides and the steel matrix, as illustrated in Fig. 5c, d, some granular voids were observed with weak signals of oxides, sulphides, and silicates. These may be attributed to the residual debris of the oxides and silicates. These are 'hard' phases and may have separated from the steel matrix during the tensile test or been removed during the subsequent sample preparation. However, the EDX signal of the MnS inclusions was strong, as indicated in Fig. 5g. This is probably due to the greater compatibility between the MnS inclusions and the steel matrix.

In the longitudinal section of Billet 2, no secondary cracking was observed, as shown in Fig. 5b, indicating that Billet 2 was less ductile than Billet 1. The fracture occurred and propagated rapidly along the primary crack without triggering any visible secondary cracks. On investigating the crack propagation, MnS inclusions were found along the crack tip, which suggests that the MnS inclusions accelerated the crack propagation and determined the crack propagating route. This supports previous studies, which have found that MnS inclusions increase the anisotropy of ductility, as observed by Pickering [23], Holappa and Helle [20] and Bhadeshia and Honeycombe [12].

Characterisation of inclusions

The inclusions present in the two as received billets, both before and after the heat treatment (heated to 1080 °C and water quenched), are compared in Figs. 6 and 7. Before the heat treatment, both elongated and granular defects were observed in the two billets, as depicted in Fig. 6a, b. Figure 6c, d presents individual typical granular and elongated inclusions as found in the two billets. The granular defects were identified to be oxides, such as Al_2O_3, MgO, and CaO (Fig. 6f), while the elongated ones were mostly made

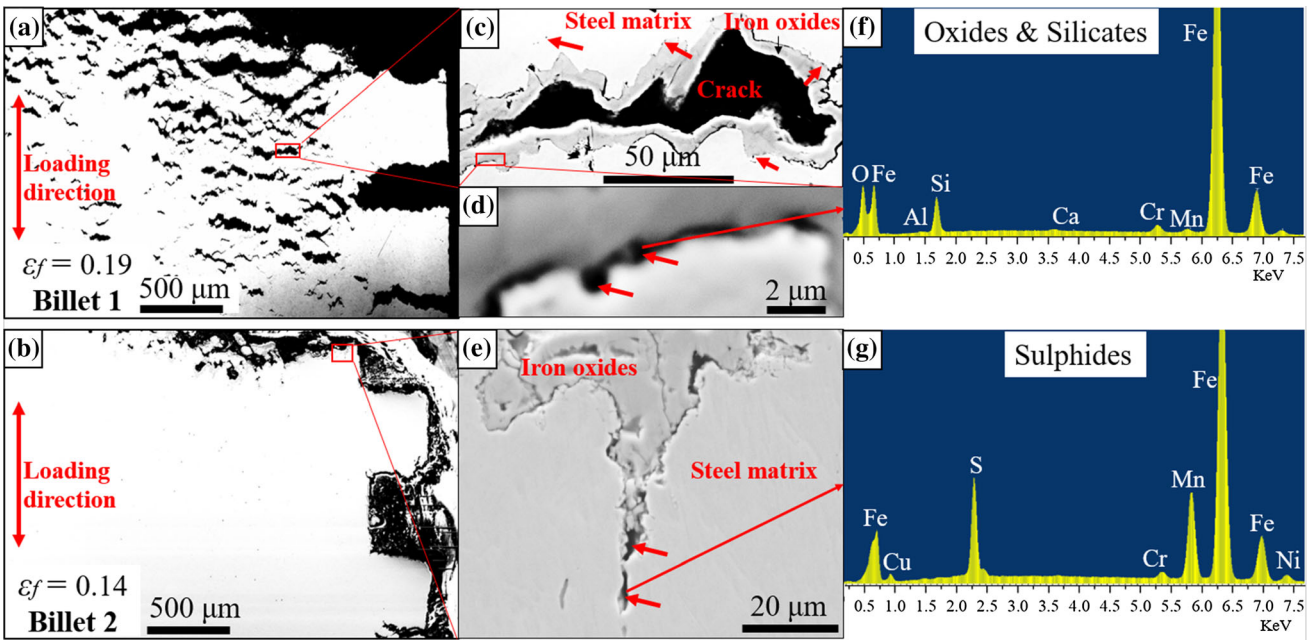

Figure 5 Microstructure of the longitudinal section of specimens after tensile tests at 1080 °C: **a**, **b** macrostructure of Billets 1 and 2 at the fracture tips; **c**, **d** one crack in Billet 1 at various magnifications; **e** crack propagation in Billet 2; **f**, **g** typical inclusions in Billets 1 and 2.

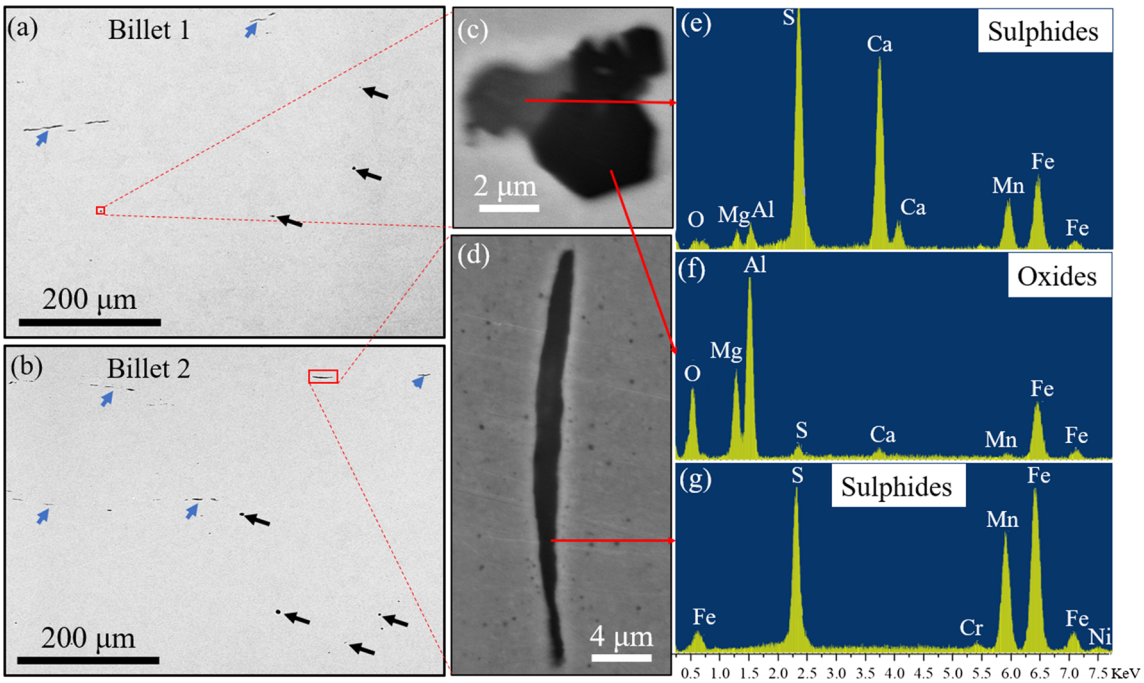

Figure 6 Inclusions distribution and identification in the two as-received billets: **a**, **b** backscattered images showing inclusions in Billets 1 and 2; **c**, **d** typical inclusions in Billets 1 and 2; **e**–**g** chemical compositions of the typical inclusions.

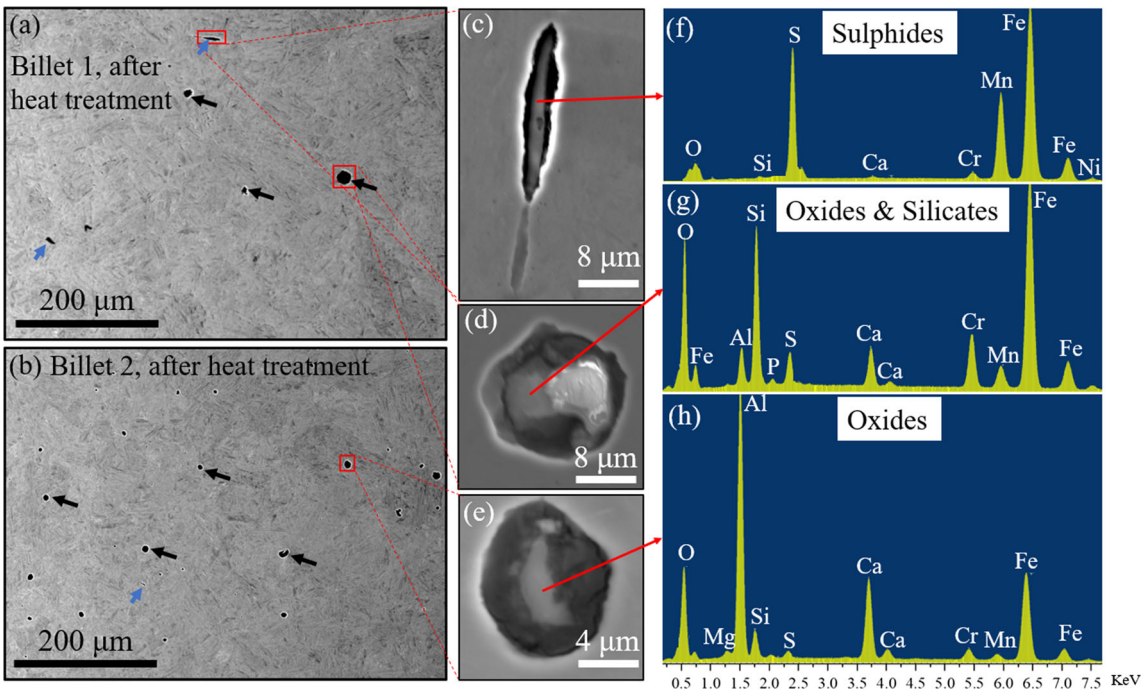

Figure 7 Inclusions distribution and identification in the two billets after heat treatment: **a**, **b** backscattered images show impurities in Billets 1 and 2 after heat treatment; **c**–**e** typical inclusions in Billets 1 and 2 after heat treatment; **f**–**h** chemical compositions of the typical inclusions.

by sulphides, such as MnS (Fig. 6g). MnS and CaS occasionally appeared along with the oxides, as illustrated in Fig. 6e.

After the heat treatment, the inclusions altered greatly in terms of size, number, and chemical composition, as demonstrated in Fig. 7. It can be clearly

seen from Fig. 7a, b that the size and number of inclusions increased after the heat treatment, as compared with those in Fig. 6a, b. The number of inclusions in Billet 2 was higher than that in Billet 1, whereas this trend was not observed at room temperature. As illustrated in Fig. 7c–e, large gaps were found between the inclusions and the steel matrix, while, at room temperature, they were well bonded, as shown in Fig. 6c–e. In addition, based on Fig. 7f–h, it is clear that the chemical components became more complex, with a new type of inclusion (silicates) being formed due to element diffusion at the high temperature.

In terms of the morphologies and chemical composition, there was no difference between the two billets at room temperature and at 1080 °C. However, at 1080 °C, the number and size of inclusions in Billet 2 was notably higher than in Billet 1.

A quantitative comparison of the inclusion histograms for the two billets is presented in Fig. 8. The histograms show that there were more small inclusions and less large ones in all samples. Comparison of the inclusions in Billets 1 and 2 reveals that the number of inclusions in Billet 2 was always higher than that of Billet 1, both with or without heat treatment, and in nearly all inclusion size ranges. The heat treatment significantly increased the number of inclusions in Billet 2, especially inclusions sized between 0 and 40 μm^2. This number was nearly three times of that in Billet 1, which suggests that the slight difference in inclusion quantity at room temperature became significantly enlarged at elevated temperature.

Characterisation of chemical and phase compositions and grain size

Figure 9 presents the chemical components of elements Cr, Mn, and Ni in the two billets and compares them with the specification. The difference in the element content between the two samples was minimal. The results also indicate that each element was uniformly distributed from the centre to the edges in both billets, and that all chemical content was within specification. This confirms that chemical composition and distribution were in close agreement with the specification provided by the steel supplier.

Figure 10 displays the distribution and components of the phases in the two billets before and after the heat treatment. The phase components of the four samples were consistent, containing ferrite, cementite, and austenite. However, the phase fractions between the two samples significantly differed before the heat treatment, as evidenced in Fig. 10a, b. In Billet 1, the percentage of ferrite was as high as 95.58%, with a tiny amount of cementite and austenite, while, in Billet 2, the percentage of austenite reached 23.38%. A significant difference in phase fraction may lead to different microstructures at high temperature. Heat treatment was applied to allow comparison of the microstructures at the rolling temperature. The heat treatment was applied without any loading of deformation of these specimens.

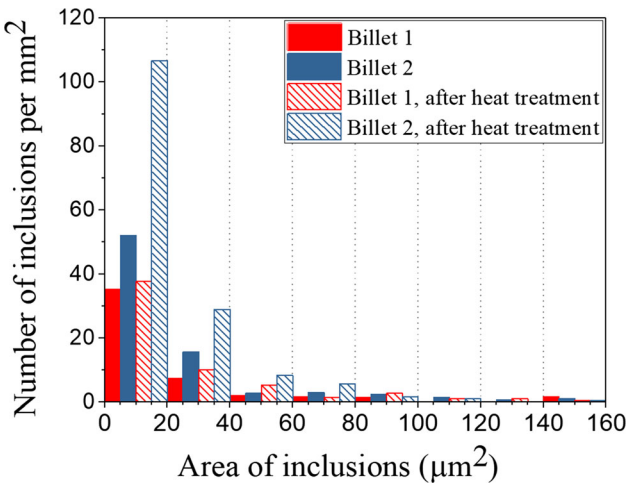

Figure 8 Histogram of inclusions in the two billets before and after heat treatment.

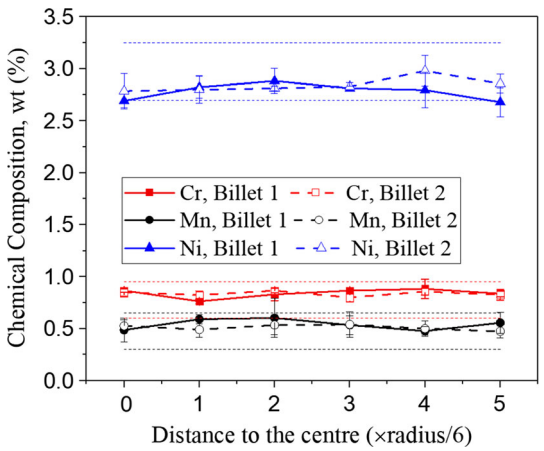

Figure 9 Chemical distribution of Cr, Mn, and Ni on the cross section of the two billets (dashed lines with the same colours present the requirements of the specification).

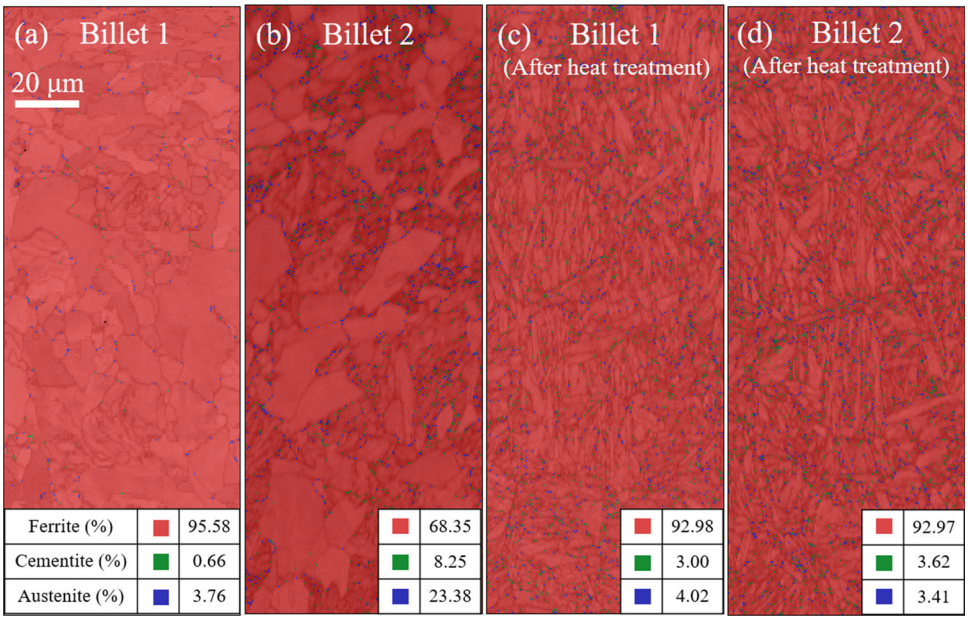

Figure 10 Phase comparisons of billets before and after heat treatment.

Figure 10c, d illustrates that the heat treatment induced homogeneous phase structures. The difference in ferrite content between two samples was as little as 0.01%. The differences in the other two phases were also minimal, because the steel was fully austenitised during the heat treatment at 1080 °C. The austenitising temperature for this steel is 850 °C.

The average grain size of the two billets before and after the heat treatment is also compared in Fig. 11. Again, only a small difference in grain size was found between the two billets. Before the heat treatment, the grain size in Billet 1 was 4.9% larger than that in Billet 2, while, after the heat treatment, the difference was reduced to 0.75%. This means that the heat treatment also reduced the difference in grain size between the two billets.

Discussion

Reasons for low hot ductility

It is widely known that for a given initial material, intrinsic factors such as inclusions, chemical

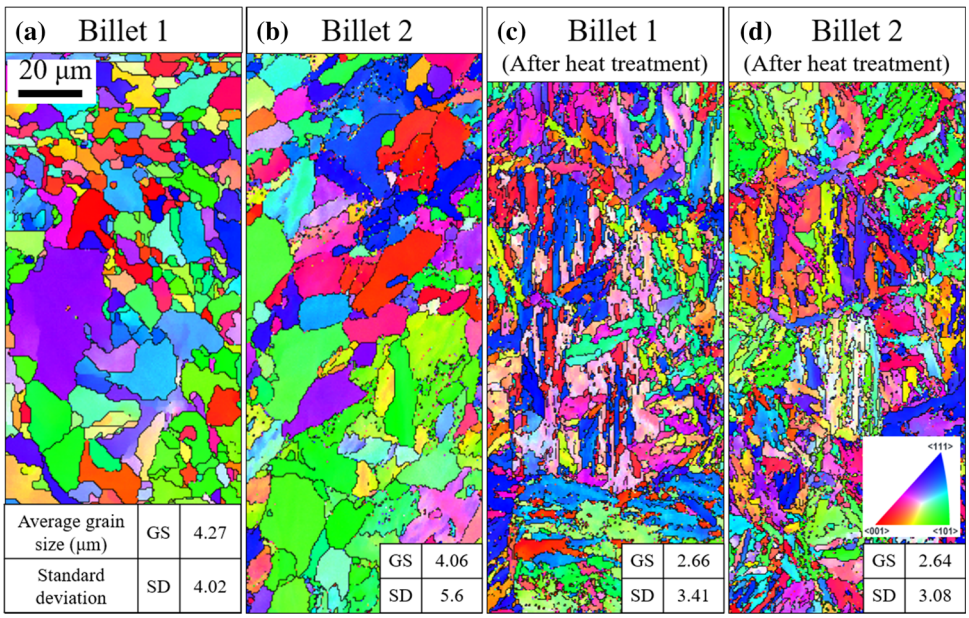

Figure 11 Grain size distribution of the two billets before and after the heat treatment.

segregation, grain size, and phase composition significantly affect ductility during subsequent hot forming. In most cases, a small grain size will improve hot ductility [25, 26, 37, 38]. High amounts of large inclusions typically have a detrimental effect on the formability of the metals and must be strictly controlled [17, 19, 39, 40]. Alloyed elements such as V and B are beneficial to the hot ductility of steel, but some elements, such as Ti, are not [41, 42]. The initial phase composition and volume fraction affect the subsequent recrystallisation and phase transformation process, as well as ductility [33]. In the work presented here, all four of these factors have been considered, analysed, and compared.

Significant differences were identified between the phase volume fractions and inclusions within the two billets in the as-received condition, as illustrated by Figs. 8 and 10a, b. These two critical microstructural factors do, however, demonstrate highly distinct trends after the heat treatment. The differences in phase volume between the two samples were significantly reduced as phase transformation resulted in homogenisation, as demonstrated in Fig. 10c, d. However, after the heat treatment, significantly more and larger inclusions were found in Billet 2 (the cracked billet) as compared to Billet 1, as shown in Fig. 8. Therefore, inclusions can be identified as potentially being the key factor responsible for central crack formation. This is consistent with the findings of Huo et al. [11] and Yang et al. [4], which state that the inclusions in CWR are considered to be a nucleation source for central cracks. This also aligns well with the general concept that inclusions are primary factors driving central crack formation [1, 7].

All other microstructural factors, such as chemical composition and grain size, exhibited little difference between the two billets. Therefore, they are highly unlikely to have resulted in the central cracks found in this study.

Inclusions evolution and crack formation

By comparing Figs. 5, 6, and 7, the inclusion evolution in terms of chemical composition, distribution, and morphologies can be seen. According to Figs. 6 and 7, it is clear that both samples experienced an increase in size and number of inclusions due to the thermal expansion and the formation of new inclusions at the high temperature. The newly formed microvoids/cracks resulted from the different thermal expansion coefficient and elasticity between the steel matrix and the inclusions. This generated stress concentration around the inclusions, and finally led to microvoid/crack formation. These microvoids/cracks became the nucleation sites for the subsequent fracture. The complicated chemical compositions of the inclusions after the heat treatment, as depicted in Fig. 7f–h, indicates that strong diffusion occurred during the heat treatment, and new inclusions, such as silicates, were generated.

The inclusions along the edges of the tensile test cracks were characterised, as shown in Fig. 5. Although the numbers of inclusions in Fig. 5f, g were not very high, oxides and silicates were observed around the crack edges and in the steel matrix. Pre-existing inclusions were still observed in the undeformed samples after the heat treatment, as shown by comparing Fig. 6a, b, (as-received) with Fig. 7a, b, (after heat treatment). The size of inclusions in Fig. 5d was small compared to the inclusions after the heat treatment. This is mainly due to the debonding between the steel matrix and the inclusions during the tensile test. Larger inclusions are more susceptible to this decohesion due to the accumulated stress between the interface with the matrix. However, the MnS is relatively soft and deformable at the high temperature, so similar numbers of MnS inclusions were still observed after the tensile test.

Under the plastic deformation, the previous microvoids/cracks in Fig. 7c, e grew and coalesced along the direction normal to the loading direction, as illustrated in Fig. 5a. Meanwhile, as the plastic deformation proceeded, new microvoids/cracks formed as a result of inclusions fracture, debonding between inclusions and steel matrix, or damage to the steel matrix [16]. With increasing plastic deformation, the voids/cracks quickly propagated the crack and led to fracture.

In summary, during the heat treatment process, element diffusion, new inclusion formation, and inclusion growth occurred simultaneously. Microvoids/cracks were formed. During the tensile test, these microvoids/cracks then grew and coalesced, and finally lead to fracture during the plastic deformation process.

Fracture mechanisms in CWR

The embrittlement resulting in premature fracture during the hot tensile test, depicted in Fig. 4c, d,

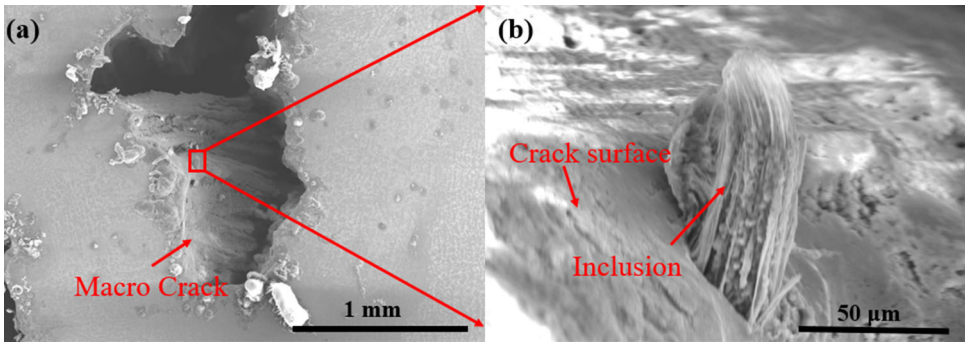

Figure 12 Cracked sample **a** macro crack; **b** inclusions on the crack surface.

occurred when the Gleeble 3800 was used to replicate the CWR process. Previous studies demonstrated that the steel experienced a ductility drop at a temperature ranging from 900 to 1200 °C, which was suggested as being due to the aggregation of sulphites and oxides at grain boundaries [19, 43]. The inclusions, such as oxides and sulphides, observed in Fig. 4c, d, are considered to be the dominant factor responsible for the low ductility.

At elevated temperature, microvoids/cracks are formed at the inclusion-steel matrix interface due to the accumulated thermal stress generated by a mismatch between the thermal expansion coefficients of inclusion and matrix. Simultaneously, grain boundary and phase boundary migration occur during the associated recrystallisation and phase transformation, thus resulting in the aggregation of inclusions adjacent to the grain boundaries. This reduces the grain boundaries' strength as compared to the grain interiors, facilitating crack propagation along grain boundaries, as shown in Fig. 5c. On a microscale, the crack propagation direction was controlled by the grain boundaries or inclusions, as indicated in Fig. 5e, whereas, on a macroscale, the overall direction was determined by the stress state, as depicted in Fig. 5a, b. As further deformation was imposed during this CWR simulation process, micro- and macrocracks formed and propagated, leading to the final fracture of the material.

The inclusions in Billet 2 were denser and larger than those in Billet 1, as seen in Fig. 8. At the CWR temperature, the difference in the inclusions size and quantity was enlarged because the thermal process facilitated to revealing the edges of the initial inclusions (e.g. MnS) due to the their thermal coefficient mismatch with the matrix materials, and the formation of new inclusions (e.g. silica) caused by fast diffusion and chemical reaction. The high quantity of inclusions in Billet 2 accelerated the element concentration and facilitated the formation of new inclusions [44–46]. The large-sized inclusions facilitated crack initiation, while the large volume fraction of inclusions accelerated the crack propagation along the grain boundary. As illustrated in Fig. 3, this resulted in the premature fracture in Billet 2, as demonstrated by the billet's lower ductility.

Furthermore, in industry, the loading condition on the workpiece is much more complex, as studied in the previous work [5], being subjected to triaxial stress state, cyclic loading, and large plastic strain. This complex loading condition accelerates the decohesion between the inclusion and steel matrix. Figure 12 shows one large inclusion on the crack surface. More detailed discussion on the important role of inclusions in cracking formation during the CWR was presented in Ref [4]. It demonstrated that the inclusions provided the nucleation sites for void formation, and generated strong localised stress causing void coalescence, and finally formed macroscopic cracks under continuous growth and coalescence. Due to the specific loading conditions and the specific fracture mechanism (shear cracking), the material in the CWR process is sensitive to inclusions. Therefore, to produce crack-free products, it is necessary to establish standards to specify the inclusion quantity and size in the CWR billet.

Conclusions

Central cracks in CWR were observed in one of two 20CrNi3H steel billets, both billets having the same chemical composition. These two billets were studied by experimentally simulating the CWR process in a tensile test using a Gleeble 3800 testing machine. The

microstructure of samples taken from the two billets was characterised under various thermal and mechanical conditions. The primary reason for the central cracking was identified, and a fracture mechanism was suggested. The following conclusions can be drawn:

1. Non-metallic inclusions, including oxides, sulphides, and silicates, are the critical factors for central crack formation in the CWR of 20NiCr3H steels. The effect of the steel chemical composition, phase composition, and grain size were found to be less critical in this case.
2. At the CWR temperature, the number and size of inclusions in the steels are enlarged, and microvoids/cracks initiate around the inclusions. Under the plastic deformation, microvoids/cracks propagate along the inclusions, and the presence of sulphides accelerates the crack propagation and leads to the material anisotropy. The ostensibly compressive conditions in CWR make the material more sensitive to inclusions.
3. The premature fracture in steel Billet 2 (inclined to central cracking) could be attributed to the inclusions introducing grain boundary embrittlement, as they tend to aggregate along the grain boundary during the recrystallisation at elevated temperature.
4. Compared to other conventional forging processes, a stricter standard on inclusions is required for the billets used for CWR to produce qualified products due to the specific loading condition.

Acknowledgements

Much appreciated is the strong support received from Beijing Institute of Aeronautical Materials (BIAM). The research was performed at the BIAM-Imperial Centre for Materials Characterisation, Processing and Modelling at Imperial College London. The authors also gratitude the financial support from the Royal Society-Newton Mobility Grant (IECNSFC181520). Xianyan Zhou acknowledges the Chinese Scholarship Council (Grant No.: 201606950020) for her bursary.

Data availability

This article has no additional data. All experimental and numerical results are reproducible.

Compliance with ethical standards

Conflict of interest The authors declare that they have no conflict of interest.

References

[1] Fu XP, Dean TA (1993) Past developments, current applications and trends in the cross wedge rolling process. Int J Mach Tools Manuf 33:367–400. https://doi.org/10.1016/0890-6955(93)90047-X

[2] Pater Z (1998) A study of cross wedge rolling process. J Mater Process Technol 80–81:370–375. https://doi.org/10.1016/S0924-0136(03)00212-7

[3] Pater Z, Tomczak J, Bulzak T et al (2019) Prediction of crack formation for cross wedge rolling of harrow tooth preform. Materials (Basel) 12:2287. https://doi.org/10.3390/ma12142287

[4] Yang C, Dong H, Hu Z (2018) Micro-mechanism of central damage formation during cross wedge rolling. J Mater Process Technol 252:322–332. https://doi.org/10.1016/j.jmatprotec.2017.09.041

[5] Zhou X, Shao Z, Pruncu CI et al (2020) A study on central crack formation in cross wedge rolling. J Mater Process Technol. https://doi.org/10.1016/j.jmatprotec.2019.116549

[6] Dong Y, Tagavi KA, Lovell MR, Deng Z (2000) Analysis of stress in cross wedge rolling with application to failure. Int J

Mech Sci 42:1233–1253. https://doi.org/10.1016/S0020-7403(99)00035-1

[7] Li Q, Lovell MR, Slaughter W, Tagavi K (2002) Investigation of the morphology of internal defects in cross wedge rolling. J Mater Process Technol 125–126:248–257. https://doi.org/10.1016/S0924-0136(02)00303-5

[8] Pater Z (2014) Cross-wedge rolling. Elsevier, Amsterdam

[9] Zhu C, Zhang H, Zhou X et al (2018) Personal communication, Laiwu

[10] Wang M, Li X, Du F, Zheng Y (2005) A coupled thermal-mechanical and microstructural simulation of the cross wedge rolling process and experimental verification. Mater Sci Eng A 391:305–312. https://doi.org/10.1016/j.msea.2004.08.080

[11] Huo Y, Lin J, Bai Q et al (2017) Prediction of microstructure and ductile damage of a high-speed railway axle steel during cross wedge rolling. J Mater Process Technol 239:359–369. https://doi.org/10.1016/j.jmatprotec.2016.09.001

[12] Bhadeshia H, Honeycombe R (2017) Steels: microstructure and properties, 4th edn. Elsevier, Amsterdam

[13] Pineau A, Amine Benzerga A, Pardoen T (2016) Failure of metals III: fracture and fatigue of nanostructured metallic materials. Acta Mater 107:508–544. https://doi.org/10.1016/j.actamat.2015.07.049

[14] Thornton PA (1971) The influence of nonmetallic inclusions on the mechanical properties of steel: a review. J Mater Sci 6:347–356. https://doi.org/10.1007/PL00020378

[15] Bartosiaki BG, Pereira JAM, Bielefeldt WV, Vilela ACF (2015) Assessment of inclusion analysis via manual and automated SEM and total oxygen content of steel. J Mater Res Technol 4:235–240. https://doi.org/10.1016/j.jmrt.2015.01.008

[16] Park JH, Kang Y (2017) Inclusions in stainless steels—a review. Steel Res Int 88:1700130. https://doi.org/10.1002/srin.201700130

[17] Luiz A (2018) Non-metallic inclusions in steels—origin and control. J Mater Res Technol 7:283–299

[18] Bielefeldt WV, Vilela ACF (2015) Study of inclusions in high sulfur, al-killed ca-treated steel via experiments and thermodynamic calculations. Steel Res Int. https://doi.org/10.1002/srin.201400112

[19] Tervo H, Kaijalainen A, Pikkarainen T et al (2017) Effect of impurity level and inclusions on the ductility and toughness of an ultra-high-strength steel. Mater Sci Eng A 697:184–193. https://doi.org/10.1016/j.msea.2017.05.013

[20] Holappa LEK, Helle AS (1995) Inclusion control in high-performance steels. J Mater Process Technol. https://doi.org/10.1016/0924-0136(95)01974-J

[21] Mu W, Dogan N, Coley KS (2018) In situ observation of deformation behavior of chain aggregate inclusions: a case study for Al_2O_3 at a liquid steel/argon interface. J Mater Sci 53:13203–13215. https://doi.org/10.1007/s10853-018-2557-0

[22] Ma W, Bao Y, Wang M, Zhao L (2014) Effect of Mg and Ca treatment on behavior and particle size of inclusions in bearing steels. ISIJ Int 54:536–542. https://doi.org/10.2355/isijinternational.54.536

[23] Pickering FB (1978) Physical metallurgy and the design of steels: austenitic stainless steels. Applied Science Publishers, Michigan

[24] Tomita Y (1993) Improved fracture toughness of ultrahigh strength steel through control of non-metallic inclusions. J Mater Sci 28:853–859. https://doi.org/10.1007/BF00400864

[25] Crowther DN, Mintz B (1986) Influence of grain size and precipitation on hot ductility of microalloyed steels. Mater Sci Technol 2:1099–1105. https://doi.org/10.1179/mst.1986.2.11.1099

[26] Mintz B, Yue S, Jonas JJ (1991) Hot ductility of steels and its relationship to the problem of transverse cracking during continuous casting. Int Mater Rev 36:187–220. https://doi.org/10.1179/imr.1991.36.1.187

[27] Kim TK, Jang J, Ryu WS et al (2001) Influence of precipitation and grain size on the hot ductility of alloy C-276 ESR ingots. High Temp Mater Process 20:143–154. https://doi.org/10.1515/HTMP.2001.20.2.143

[28] Faccoli M, Roberti R (2013) Study of hot deformation behaviour of 2205 duplex stainless steel through hot tension tests. J Mater Sci 48:5196–5203. https://doi.org/10.1007/s10853-013-7307-8

[29] Marder AR, Bramfitt BL (1976) The effect of morphology on the strength of pearlite. Metall Trans A. https://doi.org/10.1007/BF02642832

[30] Elwazri AM, Wanjara P, Yue S (2005) The effect of microstructural characteristics of pearlite on the mechanical properties of hypereutectoid steel. Mater Sci Eng A. https://doi.org/10.1016/j.msea.2005.05.051

[31] Kammerhofer C, Hohenwarter A, Scheriau S et al (2013) Influence of morphology and structural size on the fracture behavior of a nanostructured pearlitic steel. Mater Sci Eng A. https://doi.org/10.1016/j.msea.2013.07.032

[32] Kulakov M, Poole WJ, Militzer M (2013) The effect of the initial microstructure on recrystallization and austenite formation in a DP600 steel. Metall Mater Trans A Phys Metall Mater Sci 1:1. https://doi.org/10.1007/s11661-013-1721-z

[33] Zheng C, Raabe D (2013) Interaction between recrystallization and phase transformation during intercritical annealing in a cold-rolled dual-phase steel: a cellular automaton model. Acta Mater. https://doi.org/10.1016/j.actamat.2013.05.040

[34] Standardization Administration of China (2014) Structural steels with specific hardenability bands (in Chinese). GB/T 5216-2014

[35] Rasband WS (2011) ImageJ, U.S. National Institutes of Health, Bethesda. https://imagej.nih.gov/ij/

[36] Beausir B, Fundenberger JJ (2017) Analysis tools for electron and X-ray diffraction. ATEX software, Metz. http://www.atex-software.eu

[37] Hu J, Zhang JM, Sun GS et al (2019) High strength and ductility combination in nano-/ultrafine-grained medium-Mn steel by tuning the stability of reverted austenite involving intercritical annealing. J Mater Sci 54:6565–6578. https://doi.org/10.1007/s10853-018-03291-w

[38] Li J, Cao Y, Gao B et al (2018) Superior strength and ductility of 316L stainless steel with heterogeneous lamella structure. J Mater Sci 53:10442–10456. https://doi.org/10.1007/s10853-018-2322-4

[39] Zhang L, Thomas BG (2003) Inclusions in continuous casting of steel. In: XXIV national steelmaking symposium, pp 138–183

[40] Raghupathy VP, Srinivasan V, Krishnan H, Chandrasekharaiah MN (1982) The effect of sulphide inclusions on fracture toughness and fatigue crack growth in 12 wt% Cr steels. J Mater Sci 17:2112–2126. https://doi.org/10.1007/BF00540430

[41] Salas-Reyes AE, Mejía I, Bedolla-Jacuinde A et al (2014) Hot ductility behavior of high-Mn austenitic Fe-22Mn-1.5Al-1.5Si-0.45C TWIP steels microalloyed with Ti and V. Mater Sci Eng A 611:77–89. https://doi.org/10.1016/j.msea.2014.05.072

[42] Mejía I, Bedolla-Jacuinde A, Maldonado C, Cabrera JM (2011) Hot ductility behavior of a low carbon advanced high strength steel (AHSS) microalloyed with boron. Mater Sci Eng A 528:4468–4474. https://doi.org/10.1016/j.msea.2011.02.040

[43] Suzuki HG, Nishimura S, Yamaguchi S (1982) Characteristics of hot ductility in steels subjected to the melting and solidification. Trans Iron Steel Inst Jpn 22:48–56. https://doi.org/10.2355/isijinternational1966.22.48

[44] Zhang X, Yang S, Li J, Wu J (2019) Transformation of oxide inclusions in stainless steel containing yttrium during isothermal heating at 1473 K. Metals (Basel). https://doi.org/10.3390/met9090961

[45] Shibata H, Tanaka T, Kimura K, Kitamura SY (2010) Composition change in oxide inclusions of stainless steel by heat treatment. Ironmak Steelmak 37:522–528. https://doi.org/10.1179/030192310X12700328925903

[46] Chu Y, Li W, Ren Y, Zhang L (2019) Transformation of inclusions in linepipe steels during heat treatment. Metall Mater Trans B Process Metall Mater Process Sci 50:2047–2062. https://doi.org/10.1007/s11663-019-01593-1